RSC Advances

PAPER

Check for updates

Hexagonal VO$_2$ particles: synthesis, mechanism and thermochromic properties†

Hui Yan Xu, [ab] Ke Wei Xu, [ac] Fei Ma [*ab] and Paul K. Chu [*b]

Monoclinic vanadium dioxide VO$_2$ (M) with hexagonal structure is synthesized by hydrothermal method, and the phase evolution is evidenced. Interestingly, the hexagonal morphology comes into being as a result of the low-energy coherent interfaces, $(21\bar{1})_1//(2\bar{1}\bar{1})_2$ and $(2\bar{1}\bar{1})_1//(020)_2$. The size of hexagonal particles is well controlled by changing the concentration of precursor solutions. Hexagonal particles exhibit excellent thermochromic properties with a narrow hysteresis of 5.9 °C and high stability. In addition, the phase transition temperature can be substantially reduced down to 28 °C by simply W doping.

1. Introduction

Vanadium dioxide (VO$_2$) possesses several phases, M, R, B,[1] A,[2] and D,[3] and exhibits fantastic phase transition between them.[4,5] The distinguishing feature of each polymorph is the arrangement scheme of edge- or corner-sharing VO$_6$ octahedra. Monoclinic VO$_2$ (M) shows a reversible first-order metal-insulator transition (MIT) at 68 °C.[6] When the insulating VO$_2$ (M) is converted into the metallic rutile phase (R), drastic changes occur in both electrical and optical properties.[7,8] As a result, VO$_2$ has been attracting much attention owing to the potential applications in high-tech fields, such as, sensors,[9,10] catalysts,[11] lithium-ion batteries,[12] storage medium,[13] smart windows[14–17] and so on. Since the size and morphology of nanostructures affect the physical and chemical properties greatly. Therefore, it is very important to understand the formation and growth behavior of VO$_2$ and make it controllable.

A variety of physical and chemical strategies, such as, atomic layer deposition,[18] sol–gel,[19] ion implantation technique,[20] chemical vapor deposition,[21] pulsed laser deposition,[22] magnetron sputtering[23,24] and solution-based synthesis[25] have been developed to fabricate VO$_2$ nanostructures. Among them, the solution-based method gained increasing attention because of the simple preparation process and low cost. In the solution-based synthesis, VO$_2$ nanostructures of different phases and morphologies have been produced, dependent on the reaction temperature (Fig. S1†), reaction time, precursor concentration and autoclave filling ratio. Hexagonal VO$_2$ (M) was obtained by

the hydrothermal synthesis and, VO$_2$ (B), VO$_2$ (A) and VO$_2$ (D) phases appeared as intermediates. To be confused, different intermediates were involved in the hydrothermal process. VO$_2$ (B) is firstly transformed into VO$_2$ (A) and then into VO$_2$ (R).[26] However, VO$_2$ (A) does not appear in some cases.[15] Here, it is demonstrated that the hydrothermal reaction process is closely related to the reaction speed that is easily controlled by changing the concentration of precursor solutions. Hexagonal structure has been evidenced extensively, but the formation mechanism is still ambiguous. Cao *et al.*[27] proposed that it could be ascribed to the similar growth rate along the six low-energy $(20\bar{1})$ facets, while someone suggested that it was assembled from nanobelts. In this paper, the coherent relationship between each branches of hexagonal structure is characterized, which provides deep insights into the morphology evolution of VO$_2$ (M).

2. Experimental details

VO$_2$ nanostructures were synthesized by the hydrothermal method using V$_2$O$_5$ as the vanadium source and oxalic acid (H$_2$C$_2$O$_4$) as a reducing agent. The filling ratio of the vessel is about 70%. Firstly, oxalic acid (H$_2$C$_2$O$_4$) and V$_2$O$_5$ (1 : 1–1 : 3 in molar) are directly added into 35 ml deionized water at room temperature (RT), and then ammonium tungstate ((NH$_4$)$_{10}$-W$_{12}$O$_{41}$·xH$_2$O) is dispersed into the above solution and stirred for 4 hours. 35 ml of the precursor solution is transferred into a 50 ml stainless autoclave with a Teflon liner and ultimately the autoclave is heated up to 260 °C for 1–24 h and then cooled in air to room temperature. The resulting black precipitate is collected and washed with distilled water and ethanol three times by centrifugation and then dried in vacuum at 60 °C for 12 h. The as-prepared VO$_2$ nanostructures are ultrasonically dispersed in deionized water for 30 min, and an appropriate quantity of silane coupling agent KH-570 is added with ultrasonic treatment for another 30 min. Then, polyurethane (PU,

[a]State Key Laboratory for Mechanical Behavior of Materials, Xi'an Jiaotong University, Xi'an 710049, Shaanxi, China. E-mail: mafei@mail.xjtu.edu.cn

[b]Department of Physics and Materials Science, City University of Hong Kong, Tat Chee Avenue, Kowloon, Hong Kong, China. E-mail: paul.chu@cityu.edu.hk

[c]Department of Physics and Opt-electronic Engineering, Xi'an University of Arts and Science, Xi'an 710065, Shaanxi, China

DISPERCOLLU54, Bayer) is added with magnetic stirring for 10 min. Finally, the suspension is uniformly cast onto a polyethylene terephthalate (PET) substrate using an automatic coating machine and dried at 80 °C for 1 min.[30]

The morphology of VO_2 nanostructures were characterized by transmission electron microscopy (TEM) and field-emission scanning electron microscopy (FESEM, JSM-7000F). The crystal phases was determined by X-ray diffraction (GIXRD, Shimadzu XRD-7000) with Cu K$_\alpha$ radiation ($\lambda = 0.154$ nm) at a fixed incident angle of 0.5° and 2θ scanning rate of 8° min^{-1}. Differential scanning calorimetry (DSC, DSC204F1, NETZSCH, Germany) were measured at 50–100 °C with a heating rate of 5 °C min^{-1} under a nitrogen flow. The elemental component and chemical valence states were determined by X-ray photoelectron spectroscopy (Thermo Scientific K-Alpha, XPS). The transmittance spectra were measured in the range of 300–2200 nm at normal incidence using a Hitachi U-4100 spectrometer.

3. Results and discussion

Fig. 1 shows the XRD patterns of the samples prepared at three molar ratios ($r = 1, 2, 3$) of $H_2C_2O_4$ to V_2O_5. Different phase evolutions, VO_2 (B) → VO_2 (A) → VO_2 (M), VO_2 (B) → VO_2 (M) and VO_2 (B) → VO_2 (D) → VO_2 (M) are evidenced. As shown in Fig. 1a, at the reaction condition of $r = 1$, only the diffraction peaks of VO_2 (B) are identified for 1 h hydrothermal reaction. The corresponding SEM image is shown in Fig. 2a, VO_2 (B) exists in the form of nanobelts with 2–4 µm long and 200–400 nm wide. The VO_2 (B) phase is confirmed by the TEM images in

Fig. 3. The HRTEM image in Fig. 3b shows the lattice fringe spacing of 0.353 nm, corresponding to (110) lattice plane of monoclinic VO_2 (B). As illustrated by the selected area electron diffraction (SAED) pattern in the inset of Fig. 3a, the zone axis of the reciprocal lattice is [001]. If the hydrothermal reaction time is elongated to 6 h, new diffraction peaks corresponding to VO_2 (A) and VO_2 (M) phases appear on the XRD pattern, and a great number of nanobelts with rectangular ends emerge[28] (Fig. 2b). If the reaction time is further elongated to 12 h, the peaks of VO_2 (B) vanish completely and the peak intensity of VO_2 (A) and VO_2 (M) increases greatly. As displayed in Fig. 2c, rectangular nanobelts and truncated nanorods coexist. Fig. 3d presents the HRTEM image of the rectangular nanobelts in Fig. 3c, the fringe spacing of 0.59 nm matches well with the (110) plane of tetragonal VO_2 (A). According to the SEM images in Fig. 2b–d and the XRD patterns in Fig. 1a, it can be concluded that the truncated nanorods should be VO_2 (M). If the reaction time is elongated to 24 h, the peaks of VO_2 (A) become weakened gradually, but those of VO_2 (M) are enhanced, that is, the growth of VO_2 (M) rather than VO_2 (A) dominates after the elimination of VO_2 (B). At the reaction condition of $r = 2$, no peak of VO_2 (A) appears on the XRD pattern in Fig. 1b, and the size of VO_2 (B) nanostructure (Fig. 2e) is reduced substantially as compared to that in Fig. 2a. Phase transition between VO_2 (B) and VO_2 (R) was studied *in situ* by electron microscopy,[29] and it was found that VO_6 octahedra (Fig. S2†) in VO_2 (B) abruptly broke into nanocrystallites and half of VO_6 octahedra reorient into rutile structure. VO_2 (B) in spheroidal morphology appears (Fig. 2g) because of severe agglomeration. At the reaction condition of
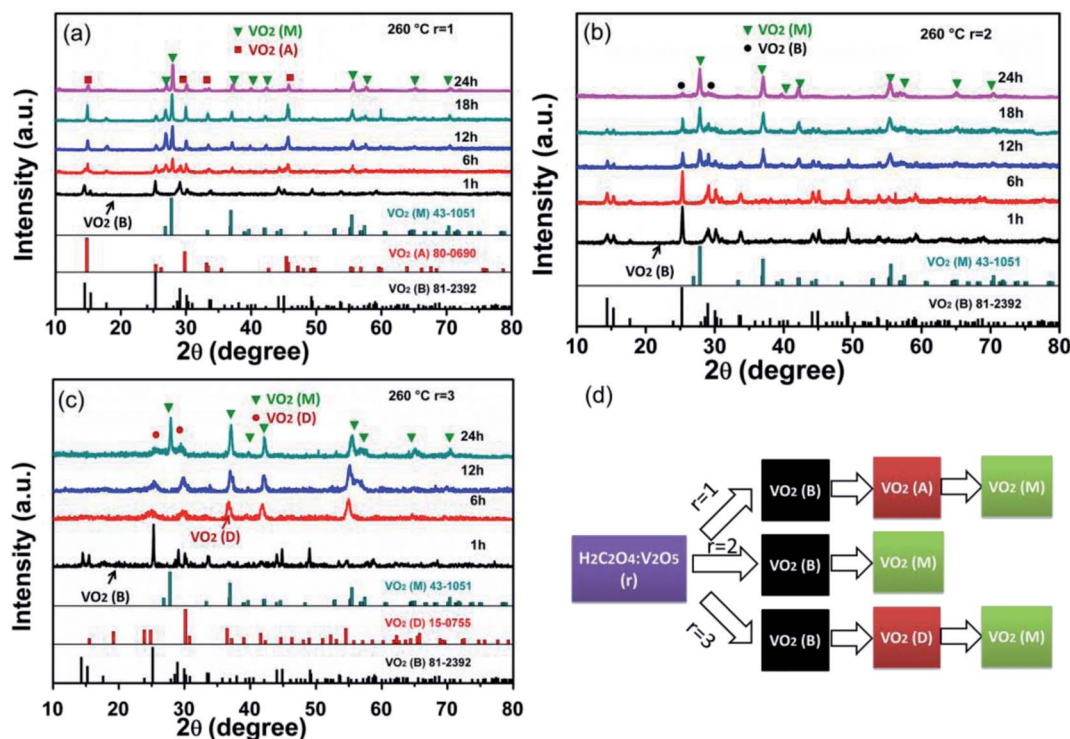

Fig. 1   XRD patterns of samples synthesized at 260 °C with different r ($H_2C_2O_4$: V_2O_5): (a) $r = 1$, (b) $r = 2$ and (c) $r = 3$; (d) the diagram of phase evolution.
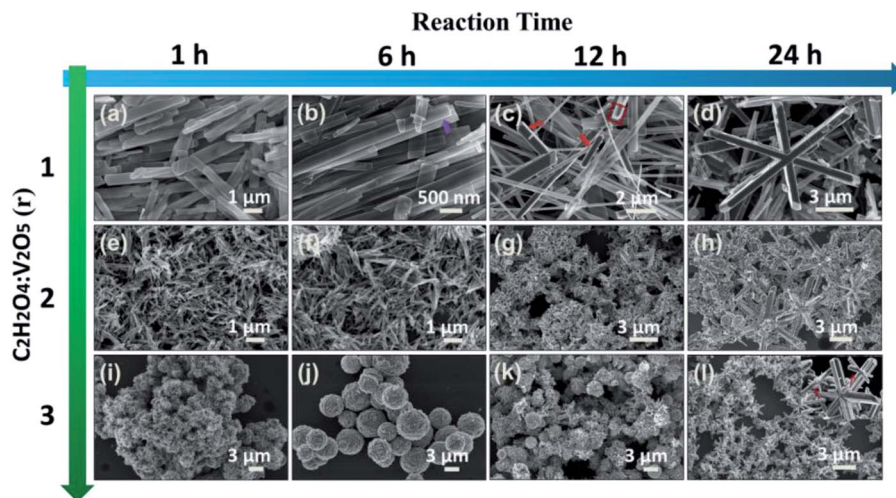
Fig. 2 SEM images of samples prepared at 260 °C under the condition of r ($H_2C_2O_4$: V_2O_5) = 1: (a) 1 h, (b) 6 h, (c) 12 h, (d) 24 h; r = 2: (e) 1 h, (f) 6 h, (g) 12 h, (h) 24 h; r = 3: (i) 1 h, (j) 6 h, (k) 12 h, (l) 24 h.

r = 3, VO_2 (B) with nanorod-like or nanobelt-like morphology (Fig. 1c) aggregate into urchin-like structures to minimize the energy.[30] Further growth leads to the formation of larger sphere-like particles as a result of Ostwald ripening (Fig. 2j). If the hydrothermal reaction time is elongated, oriented growth plays a dominant role gradually, resulting in hexagonal structure.[31] According to the XRD pattern in Fig. 1c and SEM images in Fig. 2j–k, the particles are indeed VO_2 (D) phase. The lattice fringes with a spacing of 0.372 nm corresponds to the (011) lattice plane of VO_2 (D), as shown in Fig. 3f. If the ratio of $H_2C_2O_4$: V_2O_5 is lower than 1 or higher than 3, no VO_2 (M) appears. However, pure VO_2 (A) is obtained when r is slightly lower than 1 (Fig. S3†). Cao *et al.* prepared W-doped hexagonal VO_2 (M) *via* one-step hydrothermal reactions at 240 °C for 7 days, and proposed that the hexagonal morphology was assembled by the VO_2 (M) rods along six low-index planes,[32] but they did not provide us the underlying mechanism for the formation of the hexagonal morphology. Ji *et al.* thought that the transformation from VO_2 (A) to VO_2 (M) was a resolving and re-crystallization process, and the hexagonal particles could be attributed to the electrostatic attraction.[33] However, in this work, no agglomeration and melting behavior are observed during the transformation from VO_2 (A) into VO_2 (M), but the ultra-long VO_2 (A) belts are broken into truncated VO_2 (M) rods, and hexagonal morphology of VO_2 (M) is formed through an epitaxial growth taking the center regions of rods as the nucleation sites [Fig. 2c and d].

Fig. 4 presents the TEM images of VO_2 nanostructure with hexagonal morphology. The lattice spacings of 0.242, 0.230 and 0.242 nm in Fig. 4b correspond to ($2\bar{1}\bar{1}$), (020) and ($21\bar{1}$) planes of VO_2 (M), respectively. The SAED pattern from an individual nanorod (Fig. 4d) is indexed to monoclinic VO_2 with a zone axis of [102]. The diffraction pattern does not change as the electron beam is moved along the nanobelt, characteristic of single-crystal feature. The experimental result is well consistent with the calculated SAED pattern in Fig. 4d. The SAED pattern shows

that the growth is along [100] direction. As depicted in Fig. 4e, bud-like nanoparticles grow outwards from a nanorod, in which $(21\bar{1})_1//(2\bar{1}\bar{1})_2$ and $(2\bar{1}\bar{1})_1//(020)_2$ coherent interface exist in the adjacent branches, thus small lattice distortions emerge if they are combined into a heterogeneous interface. It is demonstrated
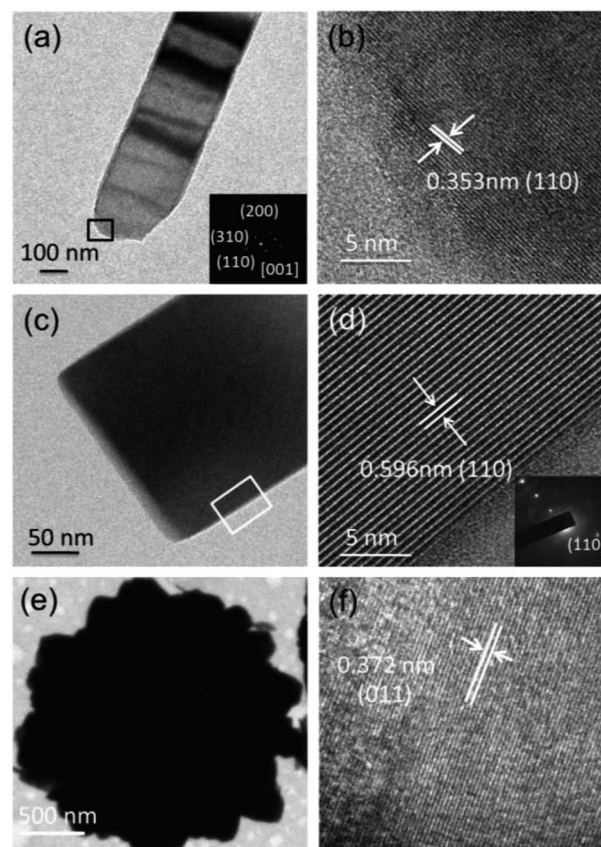

Fig. 3 (a), (c) and (e) low-resolution TEM image of VO_2 (B), VO_2 (A) and VO_2 (D), respectively. (b), (d) and (f) corresponding to the HRTEM images.
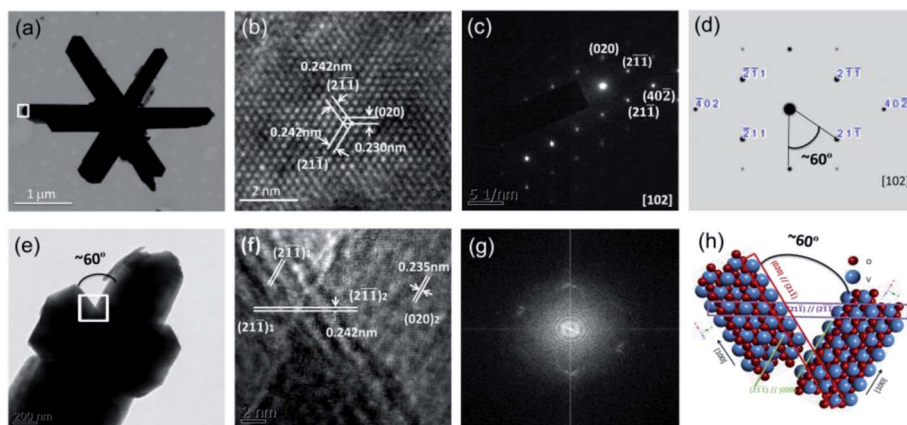
Fig. 4 (a) Low-magnification TEM images, (b) HRTEM image at the VO$_2$ rod end, (c) SAED pattern of the particle in (b) and (d) the calculated SAED pattern from [102] zone axis, (e) low-magnification TEM image, (f) HRTEM image of the overlap region between adjacent branches, (g) the FFT pattern of the overlap region from panel (f) and (h) the atomic arrangement in panel (f).

that the angle (about 60°) between the adjacent branches is decided by the coherent interfaces. The overlapped FFT patterns in Fig. 4g confirm the coherent crystalline planes between the adjacent branches, and Fig. 4h schematically shows the atomic arrangement.

Fig. 5 schematically shows the evolution of VO$_2$ (M) hexagonal morphology. The reaction proceeds toward the lowest energy, and promotes the oriented attachment.[34] Firstly, V$_2$O$_5$ is reduced by H$_2$C$_2$O$_4$ and the interphase VO$_2$ (B) is produced. As the reaction proceeds, oriented attachment or aggregation occurs spontaneously in order to minimize energy,[35] thus a great number of belts (Fig. 2b) or urchin-like (Fig. 2i) structure appear. Then metastable VO$_2$ (B) transforms into a more stable phase gradually. As aforementioned, different growth processes yield different interphases, which are dominated by nucleation rate and growth rate. H$_2$C$_2$O$_4$ plays an important role in reduction rate and further affects the supersaturation. The ratio of growth rate to nucleation rate is high under low supersaturation condition and *vice versa* (Fig. S4†). In another word, the competition between nucleation rate and growth rate results in different morphologies, high nucleation rate results in aggregation and high growth rate leads to ultra-long nanobelts. VO$_2$ (A) is from the stack of VO$_2$ (B) nanobelts. At high nucleation rate, VO$_2$ (B) prefers to aggregation rather than stacking,[36,37] and thus no VO$_2$ (A) appears. Hydrothermal reaction condition of

$r = 1$ (Fig. 2d) yields large hexagonal structure with ultra-long branches in the range of 4–8 μm and 600 nm in width. The length decreases to 4–6 μm ($r = 2$) and 2–4 μm ($r = 3$) respectively with increasing H$_2$C$_2$O$_4$. VO$_6$ octahedra of VO$_2$ (B) is different from VO$_2$ (R), but similar to VO$_2$ (A) (Fig. S2†). Thus, more energy is needed for the transformation from VO$_2$ (B) to VO$_2$ (R) ($r = 2$) than to VO$_2$ (A) ($r = 1$). So an appropriate H$_2$C$_2$O$_4$ could promote the formation of VO$_2$ (R).

Fig. 6a shows the DSC curves of the as-synthesized VO$_2$ (M) with r of 1, 2 and 3. The DSC curves of both $r = 1$ and 2 display endothermic and exothermic profiles upon heating and cooling in the temperature range of 0–100 °C, indicating a reversible phase transition,[38] but only an endothermic profile is observed in the heating process for r of 3. So the temperature range from −70 to 100 °C was adopted for the DSC measurement for r of 3, and the results are displayed in Fig. 6b. The phase transition temperature and hysteresis width of the samples are summarized in Fig. 6c. Apparently, the samples exhibit dramatically different phase transition properties. The T_C is 68, 60.5 and 62.5 °C during heating process, and 61.1, 137 and −42 °C during cooling process. The hysteresis width is about 6.9, 48.6 and 104.5 °C for the as-synthesized VO$_2$ (M) particles obtained at $r = 1$, 2, 3, respectively, and the hysteresis width is not dependent on the particle size of micrometers. As shown in Fig. 7a, some residual VO$_2$ (A), VO$_2$ (B) and VO$_2$ (D) phases exist
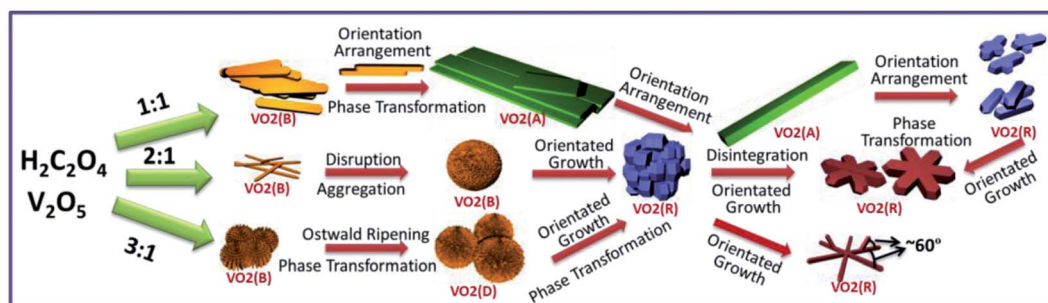

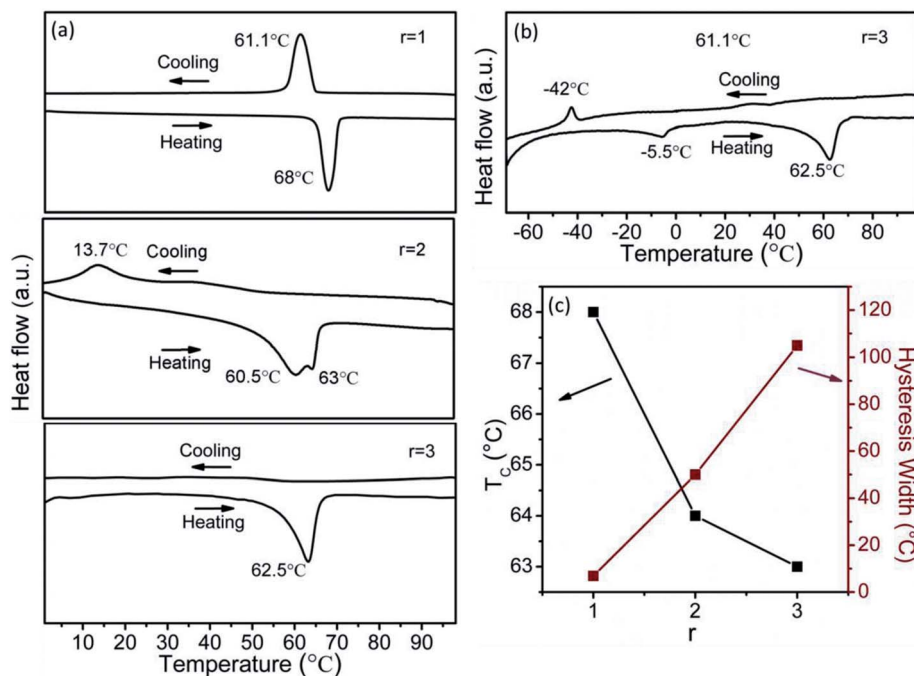**Fig. 5** Schematic evolution of the polymorph morphology.

Fig. 6 (a and b) DSC curves of the as-prepared samples, (c) T_C and hysteresis width.

except the dominating VO₂ (M) phase at r = 1, 2 and 3, respectively. The residual VO₂ (A) has little effect on the phase transition of VO₂ (M) obtained under r = 1, as shown in Fig. 6c. On the contrary, the phase evolution of VO₂ (M) obtained under r = 2, 3 is indeed a recrystallization process, and thus there is a considerable interaction between VO₂ (B) and VO₂ (M) as well as between VO₂ (D) and VO₂ (M), so the residual VO₂ (B) and VO₂ (D) affect the phase transition of VO₂ (M) obtained under r = 2 and 3. The transformation from monoclinic $(020)_M$ plane at room temperature to $(200)_R$ plane at high temperature was accompanied by the peak shift from 39.88° to 39.67°. As shown in Fig. 7b, the peak of $(020)_M$ plane shifts toward the smaller angle at r = 2 and 3. In addition, a new peak appears at 39.5° for the sample prepared under r = 3, and it is lower than 39.67°, implying increased V–V bond length and stabilized VO₂ (R) at room temperature.[39] Therefore, more energy is needed to induce the phase transition in the cooling cycle, resulting in the large hysteresis width. Fig. 9a and b show the optical transmittance of the as-synthesized and annealed samples, respectively. All the samples show a sharp optical contrast in near infrared at 20 and 90 °C. The T_{vis} and ΔT_{2000} obtained from Fig. 9a and b are displayed in Fig. 9c and d, respectively. T_{vis} changes a little but ΔT_{2000} increases significantly upon thermal annealing. It means that the residual phases affect the NIR modulation ability of VO₂ (M) considerably.

It is difficult to obtain pure VO₂ (M) in a V₂O₅–H₂C₂O₄ reaction system if no thermal annealing or doping is done.[37] As shown in Fig. 8a, pure VO₂ (M) is obtained after thermal annealing at 450 °C for 2 h. The T_C is about 70.5, 69.3 and 68 °C during the heating process, and 61.5, 61.9 and 62.1 °C during cooling process (Fig. 8b), and the hysteresis width is about 9, 7.4 and 5.9 °C when r is 1, 2 and 3, respectively. Apparently, the

hysteresis widths of the samples prepared at r = 2, 3 are reduced dramatically upon thermal annealing. But the particle size and structure changes little [Fig. S5†], indicating high stability of the hexagonal VO₂ (M). As stated above, the intermediate phases indeed have a great influence on the hysteresis width. In addition, the hysteresis width of the pure VO₂ (M) obtained here is significantly smaller than what was reported.[25,40] It can be due to the lattice distortions in coherent interface of adjacent branches. The defects act as nucleation site for metal-insulator transition and decrease the driving force. The number of branch grows as increasing r, as shown in Fig. 2, and the smallest hysteresis is obtained at r of 3.

Based on the preparation process in Fig. S6,† the composite films are prepared to measure the optical properties. The suspension composed of VO₂ (M) particles is uniformly cast on the PET substrate and the film exhibits a canary yellow color
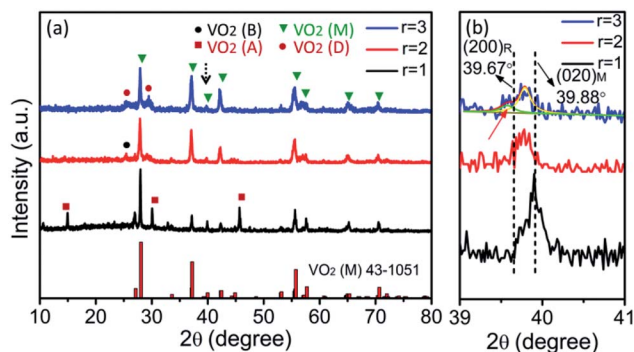

Fig. 7 (a) XRD patterns of as-prepared samples with r of 1–3, (b) magnified patterns.
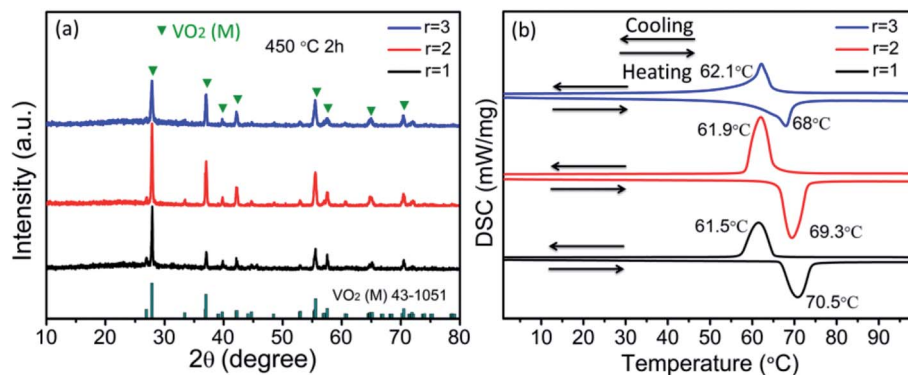
Fig. 8 (a) XRD patterns of the annealed samples (b) DSC curves of the annealed samples.

(Fig. S3b†). Fig. 9a and b show the optical transmittance of the samples before and after annealing, respectively. All the samples show a sharp optical contrast in near infrared at 20 and 90 °C, indicating that the phase transition occurs. In addition, ΔT_{2000} is continuously improved from 28.3% to 41% as r increases from 1 to 3, due to the reduced sizes of the particles.

Tungsten (W) is the most effective dopant for reducing the phase transition temperature. Fig. 10a shows a wide-range survey X-ray photoelectron spectroscopy (XPS) of W-doped VO_2 (M). C, V, W and O are detected, in which the signal of C is from the contamination on surface. From Fig. 10b, it can be seen that the $V_{2p3/2}$ peak of the particles is centered at 516.3 eV. As shown in Fig. 10c, the W4f orbital has the binding energies at 35.36 and 37.38 eV corresponding to $W_{4f7/2}$ and $W_{4f5/2}$, respectively. Accordingly, W in the powders is in the form of W^{6+}.[41] It confirms that W atoms are actually doped into the VO_2 nanoparticles. Fig. 10d shows the energy dispersive spectroscopy (EDS) of

which V, O, W and C are involved. Fig. 11a shows the DSC curves of $W_xV_{1-x}O_2$ samples with different W concentrations. Each DSC curve displays sharp endothermic and exothermic profiles upon heating and cooling cycles. In addition, the double endothermic/exothermic peaks appear during the heating/cooling process, probably due to the non-uniform doping or the polydispersity in the size distribution.[42] As shown in Fig. 10b, T_C is reduced down to 28 °C and the hysteresis width is less than 10 °C when the doping level is 2.0 at%. The substantially lowered transition temperature and small hysteresis width can meet the requirement for the applications in smart window completely. The hysteresis width is sensitive to the doping concentration.[43] However, the doped samples with hexagonal structure are more stable with a hysteresis width changing from 5 to 8 °C. In fact, the hexagonal porous morphology can provide a rigid framework and free volume simultaneously for the abrupt change between monoclinic and tetragonal phases.
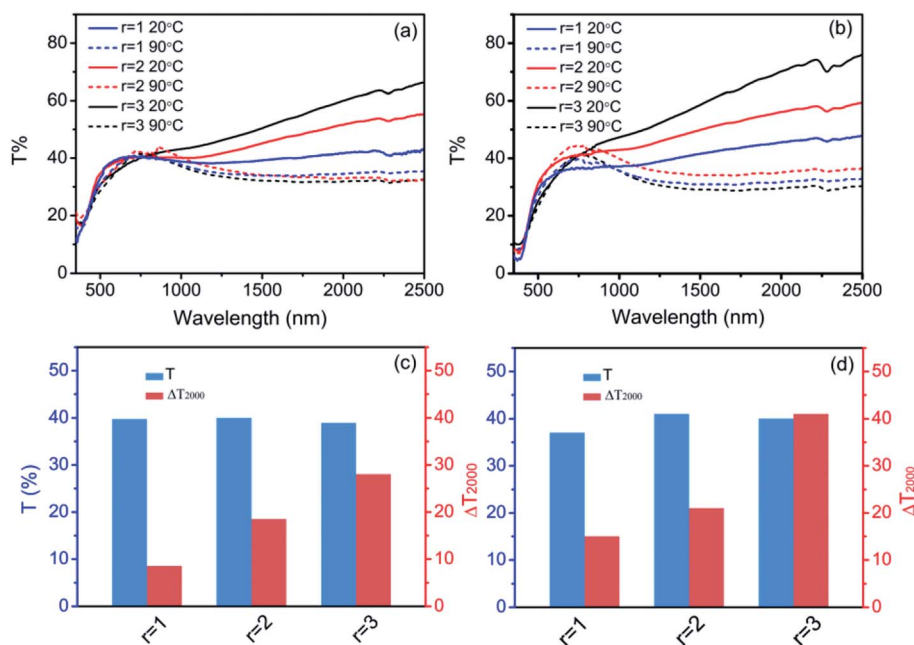

Fig. 9 Optical transmittance spectra of the (a) as-prepared and (b) annealed samples, (c and d) T_{vis} and ΔT_{2000} of the as-prepared and annealed samples, respectively.
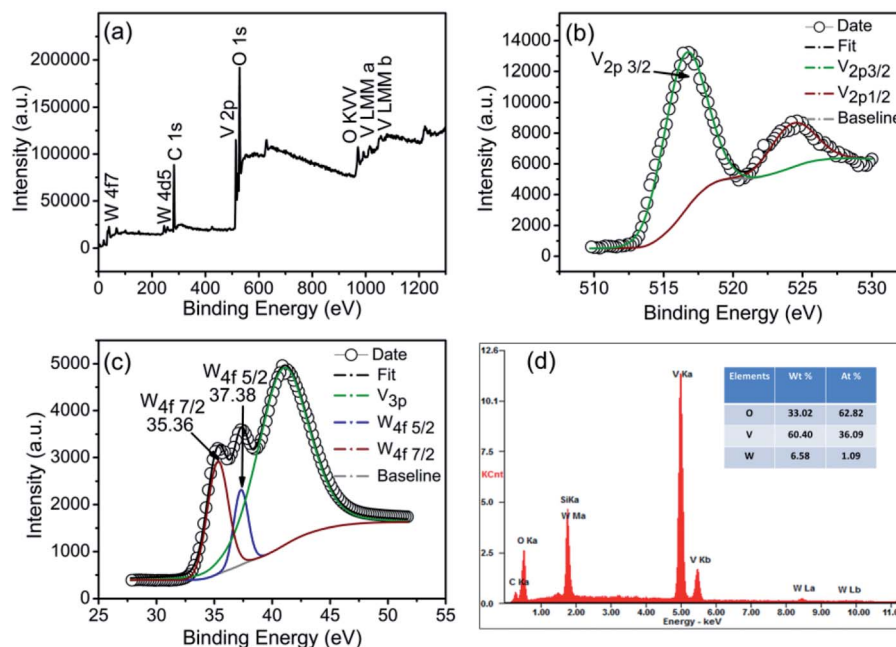
Fig. 10 (a) XPS spectra of W-doped VO_2, (b and c) high-resolution spectrum of V3p and W4f, respectively, (d) EDS spectra.
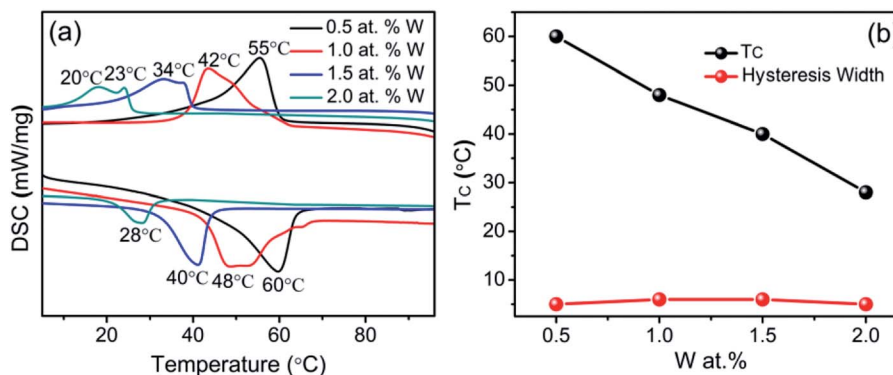

Fig. 11 (a) DSC curves of W-doped VO_2, (b) phase transition temperature and hysteresis width as a function of W doping concentration.

4. Conclusion

In summary, VO_2 (M) has been successfully synthesized through one-step hydrothermal method. $H_2C_2O_4$ plays a role in adjusting the phases and dimension of VO_2. This can be understood from the competition between the nucleation and growth rates. The coherent $((21\bar{1})_1//(2\bar{1}\bar{1})_2)$ and $((2\bar{1}\bar{1})_1//(020)_2)$ interfaces between adjacent branches promote the formation of hexagonal structure. Furthermore, it is demonstrated that the VO_2 (M) with hexagonal morphology improves the sensitivity and stability. The combination of hexagonal structure and W doping leads to substantially reduced phase transition temperature down to 28 °C.

Conflicts of interest

There are no conflicts to declare.

Acknowledgements

References

1 J. Liu, Q. Li, T. Wang, D. Yu and Y. Li, *Angew. Chem.*, 2004, **116**, 5158–5162.
2 T. Y. Y. Oka, S. Sato and N. Yamamoto, *J. Solid State Chem.*, 1998, **140**, 219.

3 L. L. B. Y. Qu, Y. Xie and B. C. Pan, *Phys. Lett. A*, 2011, **375**, 3474.

4 J. M. C. J. H. Park, T. S. Kasirga, C. Huang, Z. Fei, S. Hunter and D. H. Cobden, *Nature*, 2013, **500**, 431–434.

5 S. A. Corr, M. Grossman, Y. Shi, K. R. Heier, G. D. Stucky and R. Seshadri, *J. Mater. Chem.*, 2009, **19**, 4362.

6 G. Nie, L. Zhang, J. Lei, L. Yang, Z. Zhang, X. Lu and C. Wang, *J. Mater. Chem. A*, 2014, **2**, 2910.

7 Y. Gao, H. Luo, Z. Zhang, L. Kang, Z. Chen, J. Du, M. Kanehira and C. Cao, *Nano Energy*, 2012, **1**, 221–246.

8 Q. G. J. Wu, B. S. Guiton, N. P. de Leon, L. Ouyang and H. Park, *Nano Lett.*, 2006, **6**, 2313–2317.

9 B. Hu, Y. Ding, W. Chen, D. Kulkarni, Y. Shen, V. V. Tsukruk and Z. L. Wang, *Adv. Mater.*, 2010, **22**, 5134–5139.

10 B. Hu, Y. Zhang, W. Chen, C. Xu and Z. L. Wang, *Adv. Mater.*, 2011, **23**, 3536–3541.

11 S. Sengupta, K. Wang, K. Liu, A. K. Bhat, S. Dhara, J. Wu and M. M. Deshmukh, *Appl. Phys. Lett.*, 2011, **99**, 062114.

12 B. Sipos, M. Duchamp, A. Magrez, L. Forró, N. Barišić, A. Kis, J. W. Seo, F. Bieri, F. Krumeich, R. Nesper and G. R. Patzke, *J. Appl. Phys.*, 2009, **105**, 074317.

13 R. Xie, C. T. Bui, B. Varghese, Q. Zhang, C. H. Sow, B. Li and J. T. L. Thong, *Adv. Funct. Mater.*, 2011, **21**, 1602–1607.

14 N. Wang, S. Magdassi, D. Mandler and Y. Long, *Thin Solid Films*, 2013, **534**, 594–598.

15 J. Zheng, S. Bao and P. Jin, *Nano Energy*, 2015, **11**, 136–145.

16 C. Liu, X. Cao, A. Kamyshny, J. Y. Law, S. Magdassi and Y. Long, *J. Colloid Interface Sci.*, 2014, **427**, 49–53.

17 W. Ning, H. Yizhong, S. Magdassi, D. Mandler, L. Hai and L. Yi, *RSC Adv.*, 2013, **3**, 7124.

18 K. Martens, I. P. Radu, S. Mertens, X. Shi, L. Nyns, S. Cosemans, P. Favia, H. Bender, T. Conard, M. Schaekers, S. De Gendt, V. Afanas'ev, J. A. Kittl, M. Heyns and M. Jurczak, *J. Appl. Phys.*, 2012, **112**, 124501.

19 J. Wu, W. Huang, Q. Shi, J. Cai, D. Zhao, Y. Zhang and J. Yan, *Appl. Surf. Sci.*, 2013, **268**, 556–560.

20 S. N. P. Jin and S. Tanemura, *Thin Solid Films*, 1998, **324**, 151.

21 D. Vernardou, D. Louloudakis, E. Spanakis, N. Katsarakis and E. Koudoumas, *Sol. Energy Mater. Sol. Cells*, 2014, **128**, 36–40.

22 J. Sakai, M. Zaghrioui, V. Ta Phuoc, S. Roger, C. Autret-Lambert and K. Okimura, *J. Appl. Phys.*, 2013, **113**, 123503.

23 Y. Gao, C. Cao, L. Dai, H. Luo, M. Kanehira, Y. Ding and Z. L. Wang, *Energy Environ. Sci.*, 2012, **5**, 8708.

24 J. Zhang, J. Li, P. Chen, F. Rehman, Y. Jiang, M. Cao, Y. Zhao and H. Jin, *Sci. Rep.*, 2016, **6**, 27898.

25 Y. F. G. Z. Chen, L. T. Kang, C. X. Cao, S. Chen and H. J. Luo, *J. Mater. Chem. A*, 2014, **2**, 2718.

26 W. Yu, S. Li and C. Huang, *RSC Adv.*, 2016, **6**, 7113–7120.

27 Y. G. C. Cao and H. Luo, *J. Phys. Chem. C*, 2008, **112**, 18810–18814.

28 J. Galy, *J. Solid State Chem.*, 1999, **148**, 224–228.

29 G. N. C. Leroux and G. Van Tendeloo, *Phys. Rev. B: Condens. Matter Mater. Phys.*, 1998, **57**, 5111.

30 M. Li, D.-B. Li, J. Pan, J.-C. Lin and G.-H. Li, *Eur. J. Inorg. Chem.*, 2013, **2013**, 1207–1212.

31 M. Li, S. Magdassi, Y. Gao and Y. Long, *Small*, 2017, **13**, 1701147.

32 C. Cao, Y. Gao and H. Luo, *J. Phys. Chem. C*, 2008, **112**, 18810–18814.

33 S. Ji, F. Zhang and P. Jin, *J. Solid State Chem.*, 2011, **184**, 2285–2292.

34 L. Dai, Y. Gao, C. Cao, Z. Chen, H. Luo, M. Kanehira, J. Jin and Y. Liu, *RSC Adv.*, 2012, **2**, 5265.

35 M. Li, F. Kong, Y. Zhang and G. Li, *CrystEngComm*, 2011, **13**, 2204.

36 Z. Liu, M. Miyauchi, T. Yamazaki and Y. Shen, *Sens. Actuators, B*, 2009, **140**, 514–519.

37 J. F. L. J. T. Zhang, Q. Peng, X. Wang and Y. D. Li, *Chem. Mater.*, 2006, **18**, 867–871.

38 M. J. Powell, P. Marchand, C. J. Denis, J. C. Bear, J. A. Darr and I. P. Parkin, *Nanoscale*, 2015, **7**, 18686–18693.

39 Y. Cui, S. Shi, L. Chen, H. Luo and Y. Gao, *Phys. Chem. Chem. Phys.*, 2015, **17**, 20998–21004.

40 J. Zhu, Y. Zhou, B. Wang, J. Zheng, S. Ji, H. Yao, H. Luo and P. Jin, *ACS Appl. Mater. Interfaces*, 2015, **7**, 27796–27803.

41 G. X. X. Liu, C. Huang, Q. Xu, Y. Zhang and Y. Luo, *Mater. Lett.*, 2008, **62**, 1878–1880.

42 C. J. Patridge, L. Whittaker, B. Ravel and S. Banerjee, *J. Phys. Chem. C*, 2012, **116**, 3728–3736.

43 Y. Zhang, J. Zhang, X. Zhang, S. Mo, W. Wu, F. Niu, Y. Zhong, X. Liu, C. Huang and X. Liu, *J. Alloys Compd.*, 2013, **570**, 104–113.